
TEMPORAL EVOLUTION OF KNEE OSTEOARTHRITIS: A DIFFUSION-BASED MORPHING MODEL FOR X-RAY MEDICAL IMAGE SYNTHESIS

Zhe Wang, Mohamed Jarraya[†]

Department of Radiology
Massachusetts General Hospital
Harvard Medical School
Boston, 02114, USA
{zwang78, mjarraya}@mgh.harvard.edu

Aladine Chetouani

PRISME Laboratory, EA 4229
University of Orleans
Orleans, 45067, France
aladine.chetouani@univ-orleans.fr

Rachid Jennane

IDP Institute, UMR CNRS 7013
University of Orleans
Orleans, 45067, France
rachid.jennane@univ-orleans.fr

Yuhua Ru

Jiangsu Institute of Hematology
First Affiliated Hospital of Soochow University
Suzhou, 215006, China
ruiyuhua@163.com

Wasim Issa

Department of Orthopedic Oncology
Cancer Hospital of Pernambuco
Recife, 50040, Brazil
drwasimissa@gmail.com

August 5, 2024

ABSTRACT

Knee Osteoarthritis (KOA) is a common musculoskeletal disorder that significantly affects the mobility of older adults. In the medical domain, images containing temporal data are frequently utilized to study temporal dynamics and statistically monitor disease progression. While deep learning-based generative models for natural images have been widely researched, there are comparatively few methods available for synthesizing temporal knee X-rays. In this work, we introduce a novel deep-learning model designed to synthesize intermediate X-ray images between a specific patient's healthy knee and severe KOA stages. During the testing phase, based on a healthy knee X-ray, the proposed model can produce a continuous and effective sequence of KOA X-ray images with varying degrees of severity. Specifically, we introduce a Diffusion-based Morphing Model by modifying the Denoising Diffusion Probabilistic Model. Our approach integrates diffusion and morphing modules, enabling the model to capture spatial morphing details between source and target knee X-ray images and synthesize intermediate frames along a geodesic path. A hybrid loss consisting of diffusion loss, morphing loss, and supervision loss was employed. We demonstrate that our proposed approach achieves the highest temporal frame synthesis performance, effectively augmenting data for classification models and simulating the progression of KOA.

Keywords Knee osteoarthritis · Diffusion model · Temporal frame · Hybrid loss

1 Introduction

Knee OsteoArthritis (KOA) is a progressive disease marked by the degeneration and damage of articular cartilage, changes at the joint margins, and reactive hyperplasia of the subchondral bone [1]. Various factors, such as age, obesity, stress, and trauma, can contribute to its development [2]. Those affected often endure severe pain and limited mobility, which can greatly diminish their quality of life and elevate the risk of chronic conditions like cardiovascular disease [3]. Despite extensive research, the precise cause of KOA remains unknown, and there is currently no cure [4]. Hence, early detection is crucial for implementing timely interventions, such as weight reduction, to delay the onset and progression of KOA [5].

In 1957, Kellgren and Lawrence introduced the Kellgren-Lawrence (KL) grading system for assessing KOA [6]. According to Table 1, this system categorizes KOA into five distinct grades, determined by the presence and severity of symptoms such as osteophytes and Joint Space Narrowing (JSN). The KL grading system, despite being widely adopted, serves as a semi-quantitative method. Therefore, the diagnosis relies heavily on the practitioner’s experience and subjective judgment, which can lead to varying grades being assigned to the same knee X-ray image by different medical professionals [7].

Table 1: Detailed Overview of the KL Grading System

Grade	Severity	Detailed description
KL-0	None	Definitive absence of any osteoarthritis signs
KL-1	Doubtful	Possible presence of initial osteophytic lipping
KL-2	Minimal	Certain osteophytes formation and potential JSN
KL-3	Moderate	Multiple moderate osteophytes, confirmed JSN, some bone sclerosis, and potential bone end deformities
KL-4	Severe	Large and numerous osteophytes, confirmed JSN, and definitive deformation of bone ends

Exploring the progression of pathological changes is one of the crucial tasks in medical imaging diagnosis and planning disease treatment [8]. Particularly for KOA, which has limited effective data and is incurable in its late stages [9], generating X-ray images representing the continuous severity levels of KOA not only can simulate the progression of the disease, making the observation of its development more intuitive, but also can serve as a data augmentation technique. Especially for the KL-1 grade, which lies between healthy (KL-0) and confirmed KOA (KL-2) and is reported as doubtful KOA [10], its diagnosis presents certain challenges. During this transitional stage, the X-ray images may show subtle changes, which might be difficult to detect for medical professionals without extensive experience, yet are crucial for early diagnosis and intervention [11].

With the rapid advancements in deep learning technologies, the field of medical image generation has seen significant growth [12], particularly with the Generative Adversarial Networks (GANs) [13] and the Denoising Diffusion Probabilistic Model (DDPM) [14]. Despite their success, GAN-based models often face challenges related to training stability, including mode collapse and the complex task of finding a Nash equilibrium between the generator and discriminator [15]. This instability can hinder the model’s ability to produce diverse and realistic images, limiting its applicability in critical medical image generation tasks [16]. Conversely, the training process of DDPM, characterized by its iterative refinement of generated images through successive diffusion steps, inherently promotes the creation of high-quality and diverse samples [17], which not only mitigates the risk of generating images with artefacts or unrealistic features but also aligns closely with the nuances and complexity of medical imaging data [18].

Several diffusion-based learning models have been developed. In [19], Packhauser et al. employed a latent diffusion model [20] to generate high-quality class-conditional chest X-ray images. They introduced a sampling strategy designed to preserve the privacy of sensitive biometric information during image generation. The results demonstrated that their approach surpassed GAN-based methods. In [21], Pinaya et al. introduced a swift method utilizing DDPM for the detection and segmentation of anomalous regions in brain MRI scans. Their approach involves generating a healthy reference sample and identifying the anomaly by subtracting this generated sample from the input image to create the segmentation map. In [22], Xiang et al. emphasized leveraging conditional denoising diffusion probabilistic models for reconstructing MRI images from under-sampled data, highlighting the advantages of these models in terms of training and tuning compared to previous GAN-based methods. In [23], Jiang et al. introduced the pioneering diffusion-based model for multi-modality MRI synthesis, which features an architecture that minimizes memory usage by functioning within the latent space. In [24], Khader et al. explored the application of diffusion probabilistic models for synthesizing high-quality 3D medical images, specifically in MRI and CT imaging. The study evaluated synthetic image quality through expert radiologist assessment and demonstrated that these models can produce realistic images.

It highlighted the potential of using synthetic images in self-supervised pre-training to improve the performance of breast segmentation models, especially in situations with limited data availability.

Learning-based morphing image registration methods have been developed due to their capability to provide morphing fields in real-time, allowing the source to be transformed into the target [25]. Smooth morphing fields enable the source to morph with topology preservation [26]. Using this property, the morphed knee image might not only meet the KOA progression but also maintain all the original texture details. Drawing inspiration from the method by which DDPM produces images using the latent space derived from the parameterized Gaussian process, a novel Diffusion-based Morphing Model (DMM) to visualize the temporal evolution of KOA was proposed in this study. Specifically, our proposed approach was composed of diffusion and morphing modules. Given a source image and a target image, the latent code was learned using a score function of the DDPM. Then, this latent code was fed into the morphing module to synthesize intermediate frames through the morphing fields in an image registration manner, ensuring the topology of the source image was preserved. Moreover, to ensure that the synthesized intermediate frames corresponded more accurately to the respective KOA grade, a supervisor (i.e., a pre-trained classification model for KL-2 vs. KL-3) was introduced. Once the model was trained, continuous KOA X-rays could be synthesized from healthy knee X-ray images by averaging the morphing fields (i.e., from KL-0 to KL-1, KL-2, KL-3, and KL-4). Experimental results demonstrated that the synthesized X-ray images were valid as they effectively reflected the progression of KOA while maintaining the structural and textural integrity of the original images.

The primary contributions of this paper include the following:

- A DMM is proposed for the continuous synthesis of knee X-ray images.
- The synthesized intermediate frames are visualized to observe the progression of KOA.
- The generalization validation of the proposed approach is employed using a multi-faceted approach.
- All experimental results are sourced from the OsteoArthritis Initiative (OAI) [27] database.

2 Proposed Approach

In this section, the classical DDPM model, our proposed model, and the employed hybrid loss strategy are presented.

2.1 Classical DDPM model

Before delving into the proposed approach, we provide a brief overview of the DDPM, which serves as the foundation for our methodology.

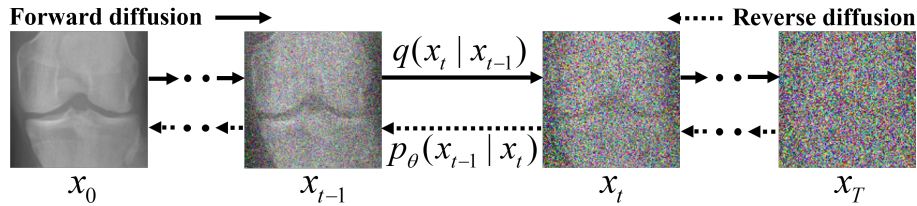


Figure 1: The structure of the classical DDPM model. The sequence from left to right shows the original X-ray image, followed by ones with increasing levels of added noise.

As shown in Fig. 1, DDPM is a generative model that aims to synthesize samples from noisy data by learning the underlying probability distribution of the clean data. At its core, the concept of DDPM revolves around modeling the evolution of data as it undergoes a diffusion process. This process involves gradually adding noise to an initial data point and then attempting to recover the original signal through denoising. By iteratively applying noise and denoising, DDPM captures the underlying probability distribution of the data, allowing them to synthesize realistic samples [28].

2.1.1 Diffusion process

A diffusion process describes the evolution of a random variable over time. Through the forward diffusion process, for the original data $x_0 \sim q(x_0)$, each step of the diffusion process, which comprises a total of T steps, involves adding Gaussian noise n to the data obtained from the previous step x_{t-1} as follows:

$$q(x_t | x_{t-1}) = \mathcal{N}(x_t; \sqrt{1 - \beta_t}x_{t-1}, \beta_t \mathbf{I}) \quad (1)$$

where β_t represents the variance used for each step in the range of $[0, 1]$, and \mathbf{I} represents the identity matrix. The entire diffusion process constitutes a Markov chain [29]:

$$q(x_1 | x_0) = \prod_{t=1}^T q(x_t | x_{t-1}) \quad (2)$$

Here, we directly sample x_t for any step t based on the original data x_0 : $x_t \sim q(x_t | x_0)$ defining $\alpha_t = 1 - \beta_t$ and $\bar{\alpha}_t = \prod_{i=1}^t \alpha_i$. Through the reparameterization technique, we have:

$$\begin{aligned} x_t &= \sqrt{\alpha_t}x_{t-1} + \sqrt{1 - \alpha_t}n_{t-1} \\ &= \sqrt{\alpha_t}(\sqrt{\alpha_{t-1}}x_{t-2} + \sqrt{1 - \alpha_{t-1}}n_{t-2}) + \sqrt{1 - \alpha_t}n_{t-1} \\ &= \sqrt{\bar{\alpha}_t}x_0 + \sqrt{1 - \bar{\alpha}_t}n, \quad \forall n_t \sim \mathcal{N}(0, \mathbf{I}) \end{aligned} \quad (3)$$

2.1.2 Denoising and Sampling

After the diffusion process, denoising is performed by sampling from the updated noise distribution. Estimating distribution $q(x_{t-1} | x_t)$ requires the utilization of the entire training set. Typically, a neural network, such as a U-Net [30], is employed to estimate these distributions. Here, the reverse process is also defined as a Markov chain composed of a sequence of Gaussian distributions parameterized by neural network parameters:

$$p_\theta(x_{0:T}) = p(x_T) \prod_{t=1}^T p_\theta(x_{t-1} | x_t) \quad (4)$$

$$p_\theta(x_{t-1} | x_t) = \mathcal{N}(x_{t-1}; \mu_\theta(x_t, t), \Sigma_\theta(x_t, t)) \quad (5)$$

where $p(x_T) = \mathcal{N}(x_T; 0, \mathbf{I})$, and $p_\theta(x_{t-1} | x_t)$ represent parameterized Gaussian distributions, with their mean $\mu_\theta(x_t, t)$ and variance $\Sigma_\theta(x_t, t)$ determined by trained learning networks.

2.1.3 Training process

The parameters θ of the diffusion module aim to minimize the distance between the true noise n and the predicted noise \hat{n} . The loss function quantifies this difference as the expected value of the squared norm between the actual noise and the noise estimated by the neural network.

$$\mathcal{L}_{diff} = \mathbb{E}_{x_0, n \sim \mathcal{N}(0, \mathbf{I})} [\|n - \hat{n}(\sqrt{\bar{\alpha}_t}x_0 + \sqrt{1 - \bar{\alpha}_t}n, t)\|^2] \quad (6)$$

where \mathbb{E} represents the expectation over the joint distribution of the original data x_0 and Gaussian noise n .

2.2 Proposed approach

As presented in Fig. 2, our approach consists of three main modules: a diffusion module, a morphing module, and a supervisor module. Source images x_S and target images x_T are a set of KL-0 and KL-4 knee X-ray images from the same individuals. Since our objective is to generate continuous frames from KL-0 image, we here define the perturbed target x_t denoting $x_0 = x_T$ according to Eq. 3:

$$x_t = \sqrt{\bar{\alpha}_t}x_T + \sqrt{1 - \bar{\alpha}_t}n \quad (7)$$

Leveraging the condition and the combination of the perturbed target x_t , the source image x_S , and the target one x_T , the latent code c is generated using the designed U-Net during the reverse diffusion. The employed 2D U-Net architecture follows a multi-scale hierarchical structure. It consists of a time embedding module, an encode module, a middle module, and a decode module. The encoder module begins with a 2D convolutional layer using a kernel size of 3 and padding of 1, followed by a series of residual blocks with increasing feature dimensions. Each residual block contains multiple convolutional layers, GroupNorm [31] for normalization, Swish activation function for non-linearity, and optional dropout for regularization. The middle module introduces self-attention modules that enable the capture of

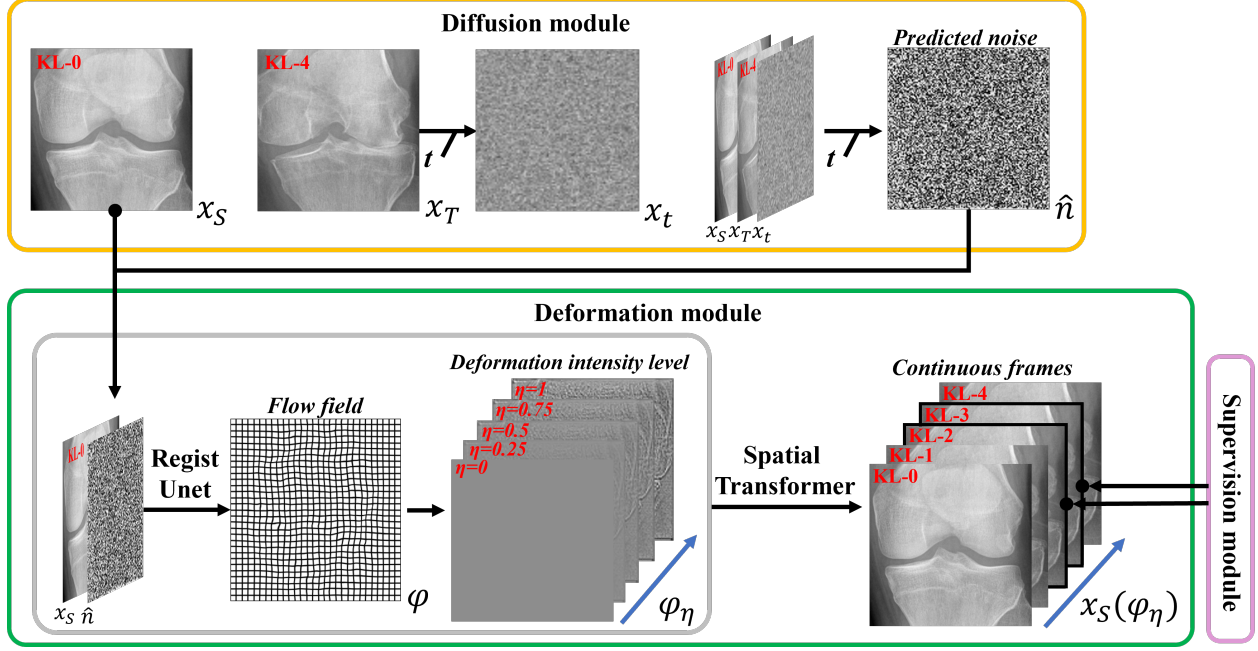


Figure 2: Flowchart of the proposed approach, with black arrows representing the data flow. First, the source x_S and target x_T knee X-ray images are fed into the diffusion module, where the source image x_T undergoes a process that adds noise to the image, incrementally increasing its noise level. Then, the source x_S , target x_T , and noised x_t images are utilized to predict the noise \hat{n} . Following the diffusion module, the predicted noise \hat{n} and the source x_S image are processed through the morphing module, which applies transformations to the images via a flow field φ to simulate structural changes. The different levels of morphing are denoted by η values. After morphing, the synthesized images $x_S(\varphi_\eta)$ are supervised by a supervision module to ensure they more accurately correspond to each stage of KOA. Further details are provided in Section 2.2.

long-range dependencies in the data. Throughout the encoder, downsampling is achieved using 2D convolutional layers with a kernel size of 3, stride of 2, and padding of 1, which effectively reduces the spatial dimensions while increasing the number of feature channels. In the decoder, residual blocks are employed again. Upsampling is performed through a combination of 2D convolutional transpose layers with a kernel size of 2, stride of 2, and padding of 0, followed by residual blocks to fuse features from the encoder and decoder pathways.

Then, the source image x_S and predicted noise \hat{n} are fed to a registration network to obtain a morphing flow field φ . The employed registration network follows a U-Net-like structure. The input block performs an initial convolution with downsampling to capture low-level features. Subsequently, a contracting path is formed using downsampling blocks that progressively reduce spatial dimensions while increasing channel complexity. On the other hand, the expansive path employs upsampling blocks to recover spatial details and enhance features. These upsampled features are then concatenated with features from the contracting path, facilitating information fusion. Before generating the final output, a refinement block refines the concatenated features. Finally, the output block generates the predicted morphing flow field φ . It is noteworthy that here we introduce a scale parameter η for the flow field φ , which represents five uniformly distributed numbers within the range $[0, 1]$ as the adjustable morphing intensity level (i.e. $\varphi_\eta = \eta\varphi$) for the synthesized intermediate frames from KL-0 toward KL-4.

After this, the source image x_S with the predicted noise \hat{n} as the latent codes c and morphing flow field φ_η are fed to the Spatial Transform Network (STN) [32]. STN is a specialized type of neural network architecture that is designed to perform spatial transformations on input data. Here, we use the bilinear interpolate and sample pixel values from the latent codes c on the generated grid, mapping them to the output image $x_S(\varphi_\eta)$ based on the morphing flow field φ .

Finally, under the supervision of the pre-trained KL-2 vs. KL-3 classifier for $x_S(\varphi_{\eta=0.5})$ and $x_S(\varphi_{\eta=0.75})$, five continuous morphed images (i.e., $x_S(\varphi_{\eta=0})$, $x_S(\varphi_{\eta=0.25})$, $x_S(\varphi_{\eta=0.5})$, $x_S(\varphi_{\eta=0.75})$, and $x_S(\varphi_{\eta=1})$) are synthesized. For more intuition, Algorithm 1 describes the training process of the proposed approach, with different constraint losses detailed in the following section.

Algorithm 1 Learning algorithm of the proposed approach

Input: x_S, x_T, t , and all initial parameters
Output: $\varphi, x_S(\varphi_\eta)$, and learned parameters
repeat
 Get $n, x_t \leftarrow \text{noise}(x_S, t)$
 Get $\hat{n} \leftarrow \text{denoise}(x_S, x_T, x_t, t)$
 Compute $\mathcal{L}_{diff}(n, \hat{n})$ ▷ Eq. 6
 Get $\varphi_\eta \leftarrow \text{morph}(x_S, \hat{n})$
 Get $x_S(\varphi_\eta) \leftarrow \text{STN}(x_S, \varphi_\eta, \hat{n})$
 Compute $\mathcal{L}_{mph}(x_S(\varphi_{\eta=1}), x_T)$ ▷ Eq. 10
 Compute $\mathcal{L}_{sup}(x_S(\varphi_{\eta=0.5}), x_S(\varphi_{\eta=0.75}))$ ▷ Eq. 11
 Update Parameters of the model
until *convergence*

2.3 Hybrid loss strategy

In the diffusion module, the diffusion loss \mathcal{L}_{diff} is defined as shown in Eq. 6. In the morphing module, drawing from the energy function used in traditional image registration, the morphing loss J_{mph} consists of Normalized Cross-Correlation (NCC) loss and Image Gradient (IG) loss. NCC calculates the correlation between two vectors of the same dimension, with values ranging from $[-1, 1]$. A value of -1 indicates no correlation between the vectors, while a value of 1 indicates perfect correlation. The NCC loss \mathcal{L}_{NCC} is defined as follows:

$$\mathcal{L}_{NCC} = 1 - \frac{\sum_{i,j} (A * B)^2}{\sqrt{\sum_{i,j} A^2 \sum_{i,j} B^2}} \quad (8)$$

where A and B represent the input and target images, respectively. $*$ denotes the cross-correlation operation. i and j are indices of the image.

On the other hand, the IG loss calculates the mean squared Euclidean distance between the gradient channels of the reference image and the target one. It encourages the two images to have similar gradient patterns, which can help in enhancing fine details or maintaining stylistic consistency between images. The IG loss \mathcal{L}_{IG} is defined as follows:

$$\mathcal{L}_{IG} = \sum_{i,j} \left| \frac{\partial A}{\partial x} - \frac{\partial B}{\partial x} \right| + \left| \frac{\partial A}{\partial y} - \frac{\partial B}{\partial y} \right| \quad (9)$$

where $\frac{\partial A}{\partial x}$, $\frac{\partial B}{\partial x}$, and $\frac{\partial A}{\partial y}$, $\frac{\partial B}{\partial y}$ are the partial derivatives of the images A and B with respect to the x -axis (horizontal gradient) and y -axis (vertical gradient), respectively.

The morphing loss J_{mph} is defined as:

$$\mathcal{L}_{mph} = \mathcal{L}_{NCC}(x_S(\varphi_{\eta=1}), x_T) + \mathcal{L}_{IG}(x_S(\varphi_{\eta=1}), x_T) \quad (10)$$

As KL grades possess a semi-quantitative nature and cannot be strictly divided into continuous intervals according to a uniform distribution, we here introduce a pre-trained classifier as a supervision module, which aims to enhance the accuracy of the KL grade assignments for intermediate frames. Since the literature often considers the label data for KL-1 patients to be questionable, these labels may involve significant uncertainties. Therefore, we focused on the supervision for the intermediate frames of KL-2 and KL-3, corresponding to the $x_S(\varphi_{\eta=0.5})$ and $x_S(\varphi_{\eta=0.75})$. To do this, the Stat-Of-The-Art (SOTA) classification model proposed in [33] was employed. The supervision loss \mathcal{L}_{sup} is calculated as:

$$\mathcal{L}_{sup} = \mathcal{L}_{CE}(x_S(\varphi_{\eta=0.5})) + \mathcal{L}_{CE}(x_S(\varphi_{\eta=0.75})) \quad (11)$$

Finally, given that the diffusion loss \mathcal{L}_{diff} is the basic function of the global approach, a weight of 1 was assigned. The proposed hybrid loss function \mathcal{L}_{hybrid} in this study is defined as:

$$\mathcal{L}_{hybrid} = \mathcal{L}_{diff} + \lambda_1 \mathcal{L}_{mph} + \lambda_2 \mathcal{L}_{sup} \quad (12)$$

where the hyper-parameters λ_1 and λ_2 serve to weigh and balance the aforementioned loss functions more effectively. The influence of these parameters on performance will be examined in Section 4.1.

3 Experimental settings

This section provides an overview of the experimental data, the preprocessing steps undertaken, and the specifics of the experimental procedures.

3.1 Employed knee database

The OsteoArthritis Initiative (OAI) [27] represents a significant and rich source of data for researchers investigating KOA and related conditions. By analyzing data from 4,796 participants aged between 45 and 79 years over 96 months, the initiative provides a comprehensive longitudinal dataset. Each participant underwent nine follow-up examinations, allowing for detailed tracking of the disease’s progression and the identification of potential risk factors associated with KOA development or progression.

3.2 Data preprocessing

The knee joints employed in this study are derived from [34]. As shown in Fig. 3, the knee joint (Fig. 3(b)) was identified from the plain radiograph (Fig. 3(a)) through the YOLOv2 learning model [35], with images sized 299×299 , which were resized to 224×224 pixels, and image intensity was normalized to $[-1, 1]$. As a result of the preprocessing steps, 60 pairs of KL-0 and KL-4 images were collected from the baseline, 24-month, 36-month, 48-month, 72-month, and 96-month datasets. Each X-ray image pair was obtained from the same patient, ensuring consistency in the temporal progression of KOA within the dataset.

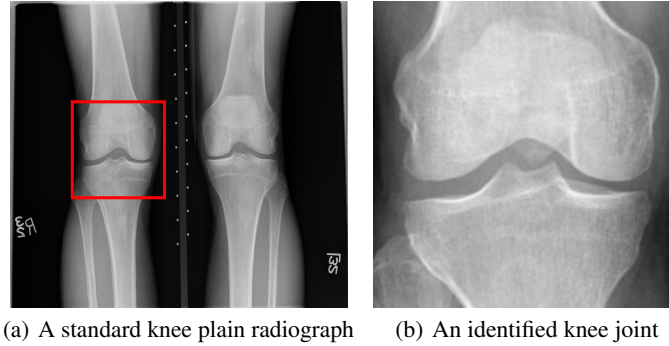


Figure 3: A standard knee plain radiograph from the database and an identified knee joint highlighted in a red box 3(a). An identified knee joint 3(b).

3.3 Experimental details

The weights of all modules (denoise network, registration network, and STN) were initialized using the Kaiming procedure [36]. To enhance the model’s generalization ability, the diffusion steps T are randomized in each epoch, with a maximum value set to 2,000. The Adam optimizer method [37] was utilized for training over 500 epochs. The training configuration included a mini-batch size of 16, with the denoise network using a learning rate of $2e-04$, and both the registration network and STN using a learning rate of $1e-05$. We implemented our approach using PyTorch v1.8.1 [38] on Nvidia H100 graphics cards with 80 GB of memory.

4 Results and discussion

This section presents and analyzes the experimental results.

4.1 Selection of the hyper-parameters

To ensure the effectiveness of generating intermediate frames in advance, the weight hyper-parameters (λ_1 and λ_2) in the proposed hybrid loss function (Eq. 12) were tuned via a small grid search over combinations of $\lambda_1 \in [0, 1]$ and $\lambda_2 \in [0, 1]$. By leveraging the supervision’s feedback, adjustments to the hyper-parameters λ_1 and λ_2 were made. To do this, we calculated the supervision loss \mathcal{L}_{sup} for the generated intermediate frames $x_S(\varphi_{\eta=0.5})$ and $x_S(\varphi_{\eta=0.75})$. As can be seen in Fig. 4, the z-axis, representing the negative log of the loss function, indicates the model performance, with higher bars suggesting better performance (i.e., lower loss). After five rounds of testing, the experimental results provided insights into the trade-offs between different hyper-parameter settings. Assigning higher values to λ_1 ensures that the intermediate frames maintain a coherent motion trajectory. However, overemphasis on λ_1 may result in neglecting fine details, reducing the accuracy of KOA characteristics. On the other hand, higher values of λ_2 compromise temporal smoothness, leading to discontinuous sequences. Ultimately, the combination of $\lambda_1 = 0.1$ and $\lambda_2 = 0.01$ was selected as the optimal weights for the hybrid loss function.

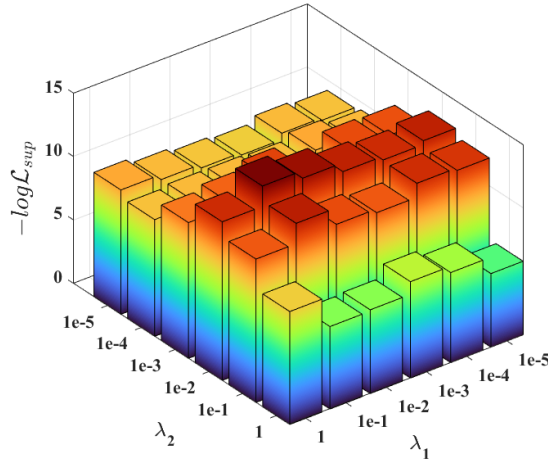


Figure 4: Supervision performance metrics obtained using different values of λ_1 and λ_2 for the synthesized intermediate frames $x_S(\varphi_{\eta=0.5})$ and $x_S(\varphi_{\eta=0.75})$.

4.2 Visualization of the synthesized intermediate frames

In Table 2, we show the source image x_S , the target image x_T , and their intermediate frames (i.e., $x_S(\varphi_{\eta=0.25})$, $x_S(\varphi_{\eta=0.5})$ and $x_S(\varphi_{\eta=0.75})$), which is crucial in understanding how the source images evolve into their registered state. The progressive alignment is quantified by the parameter η evenly divided into 0.25, 0.5, and 0.75, which represents the extent of transformation at each stage of KOA, corresponding to KL-1, KL-2, and KL-3, respectively. As can be seen, $x_S(\varphi_{\eta=0.25})$ shows the initial stage of the morphing process where the morphs are minimal and closely resemble the source image. For $x_S(\varphi_{\eta=0.5})$, the morph is more pronounced, introducing clear signs of osteophytes and beginning to show a narrowing of the joint space. It is noteworthy that this frame is critical as it represents the halfway anchor point of the KOA temporal evolution process, showing a balanced mix of characteristics from both the source and target images. $x_S(\varphi_{\eta=0.75})$ signifies an advanced stage of morph, introducing moderate multiple osteophytes, definite narrowing of the joint space, some sclerosis, and possible deformity of bone contour.

4.3 Comparison of different existing approaches

The evaluation of the intermediate frames was employed using the Peak Signal-to-Noise Ratio (PSNR) and the Normalized Mean Square Error (NMSE) according to the real images to quantify the quality of the generated morphed images. Specifically, PSNR is a measure used to assess the quality of reconstructed or compressed images compared to their original versions. Higher PSNR values typically signify improved reconstruction quality, as they indicate lower deviation from the original image. The formula for PSNR is:

$$\text{PSNR} = 10 \cdot \log_{10} \left(\frac{\text{MAX}_I^2}{\text{MSE}} \right) \quad (13)$$

Table 2: Visualization of the synthesized intermediate frames*

Input image x_S	Synthesized intermediate frames				Input image x_T
	$x_S(\varphi_{\eta=0.25})$	$x_S(\varphi_{\eta=0.5})$	$x_S(\varphi_{\eta=0.75})$		
KL-0	KL-1**	KL-2**	KL-3**	KL-4	

* The morphed areas of each frame were highlighted within black boxes, the red arrow and red circle indicate the locations of JSN and osteophyte formation, respectively. A shorter arrow indicates a smaller joint space (i.e., a narrower distance between the tibia and femur), while a larger circle indicates more osteophytes.

** The expected labels.

where MAX_I is the maximum possible pixel value of the image. MSE stands for the Mean Squared Error, which calculates the average of the squared differences between the real and synthesized images:

$$\text{MSE} = \frac{1}{mn} \sum_{i=1}^m \sum_{j=1}^n (I(i, j) - K(i, j))^2 \quad (14)$$

where $I(i, j)$ and $K(i, j)$ are the pixel values at position (i, j) in the real and synthesized images, respectively. m and n are the width and height of the image.

On the other hand, NMSE is a measure of the quality of an estimator. It normalizes the MSE by the variance of the actual values, providing a scale-independent accuracy measure. An NMSE value close to 0 indicates a model with minimal error compared to the variance of the data. The formula for NMSE is:

$$\text{NMSE} = \frac{\sum_{i=1}^n (y_i - \hat{y}_i)^2}{\sum_{i=1}^n (y_i - \bar{y})^2} \quad (15)$$

where y_i denotes the true values, \hat{y}_i signifies the predicted values, \bar{y} is the average of the true values, n represents the total number of observations.

We compared the performance of the proposed method with existing approaches, including VoxelMorph (VM) [39], VoxelMorph-diff (VM-diff) [40], and Diffusion Deformable Model (DDM) [41]. The evaluation focused on the synthesized intermediate frames (i.e., $x_S(\varphi_{\eta=0.25})$, $x_S(\varphi_{\eta=0.5})$, and $x_S(\varphi_{\eta=0.75})$) by comparing them with the corresponding real images using two key metrics PSNR and NMSE. After five rounds of testing, the box plots illustrate the statistical distribution of these metrics. As can be seen in Fig. 5, VM and VM-diff have a wider spread of PSNR values, with more variation in the results. The DDM is more consistent but generally yields lower median PSNR values than our proposed method. Especially with $x_S(\varphi_{\eta=0.5})$, our method shows a higher median PSNR and a tighter interquartile range, indicating better and more consistent image quality. On the other hand, our proposed method has a consistently lower NMSE across all three cases (i.e., $x_S(\varphi_{\eta=0.25})$, $x_S(\varphi_{\eta=0.5})$, and $x_S(\varphi_{\eta=0.75})$), which suggests a superior estimation accuracy over the compared methods. This is not only evident from the lower median values but also from the tighter interquartile ranges, implying a more reliable performance regardless of the underlying complexity characterized by φ_{η} . The DDM has higher variability in NMSE scores, especially for $x_S(\varphi_{\eta=0.25})$ and $x_S(\varphi_{\eta=0.5})$. The medians do not show a large difference between $x_S(\varphi_{\eta=0.25})$ and $x_S(\varphi_{\eta=0.5})$ across the groups, but there is a

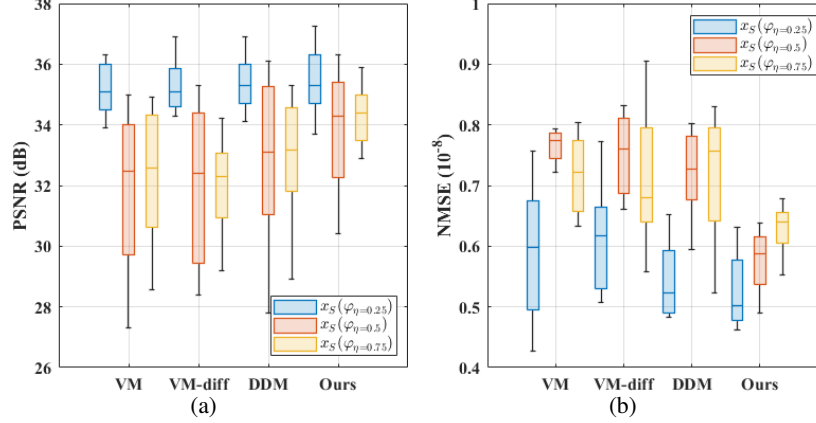


Figure 5: The box plots visualize the different performance of the selected approaches using PSNR 5(a) and NMSE 5(b) for the synthesized intermediate frames $x_S(\varphi_{\eta=0.25})$, $x_S(\varphi_{\eta=0.5})$, and $x_S(\varphi_{\eta=0.75})$.

noticeable improvement for $x_S(\varphi_{\eta=0.75})$ using our method. Overall, the box plots indicate that our proposed method not only achieves higher PSNR values, suggesting better image quality and fidelity, but also minimizes NMSE, implying more accurate predictions of intermediate frames. These results demonstrate the efficacy of our approach in synthesizing high-quality and accurate intermediate frames for KOA.

4.4 Generalization validation of the proposed approach

To verify the generalization capability of the proposed approach, during the testing phase, only patient samples with KL-0 data are used as source images x_S to synthesize continuous frames until the last frame $x_S(\varphi_{\eta=1})$. To achieve this, once the model converges, the average of the morphing fields φ from the last five iterations is calculated to obtain a unified morphing field $\bar{\varphi}$. Subsequently, the model weights are frozen to maintain this state. The synthesized frames are then evaluated using a multi-faceted approach, which aims to ensure the reliability and applicability of the synthesized frames in both clinical and research settings.

4.4.1 Data augmentation effects

To ensure that the experimental results more sensitively reflect the impact of the synthesized frames, the evaluation of the data augmentation effects was conducted via binary classification tasks. According to each classification task, we divided the corresponding dataset into a training set and validation set with the ratio of 7:3. Then, the corresponding synthesized intermediate frames were utilized as augmented data into the training set while fixing the validation set. As presented in Table 3, the selected evaluation SOTA models are from [42] and [33] using the respective configurations (i.e., same number of training epochs, same learning rate, etc.). As can be seen, the incorporation of synthesized images leads to a general improvement in accuracy for all classification tasks across both evaluation models. More specifically, for Tiulpin et al. [42], the improvements range from a modest 0.27% for the KL-1 vs KL-4 task to a more substantial 3.84 % for the KL-1 vs KL-2 task. Similarly, for Wang et al. [33], the enhancements in accuracy are also noticeable, with the KL-0 vs KL-2 task seeing a 2.54% increase and the KL-1 vs KL-2 task experiencing a 3.29 % improvement. These figures highlight a trend where the more significant enhancements are observed in classifications involving KL-2 grade. The KL-2 represents a critical grade where KOA characteristics begin to be unequivocally observed, albeit in their nascent stages. This makes the classification between the very early stages (i.e., KL-0, KL-1, and KL-2) particularly sensitive to the augmentation of data volume, as the additional nuances captured through data augmentation can significantly aid in the identification of early degenerative changes. On the other hand, for the higher grades (i.e., KL-3 and KL-4), where KOA characteristics are more pronounced and easier to be identified even with smaller datasets, the incremental improvements achieved through data augmentation are less dramatic.

4.4.2 Visualization analysis

To visualize the differences before and after incorporating synthesized frames during training, t-distributed Stochastic Neighbor Embedding (t-SNE) [43] was applied to reveal the high-dimensional feature space on the validation set and to highlight the generalization differences of the model. For better clarity, we focus on the impact of synthesized frames specifically on the KL-0 vs. KL-1 and KL-1 vs. KL-2 classification tasks, as they demonstrate the most significant

Table 3: Analysis of data augmentation effects

Model	Task	Acc (%)		Diff (%)
		Original training set	Augmented training set*	
Tiulpin et al. [42]	KL-0 vs KL-1	65.88	68.11	2.23 ↑
	KL-0 vs KL-2	87.33	89.13	1.80 ↑
	KL-0 vs KL-3	96.29	97.01	0.72 ↑
	KL-1 vs KL-2	70.33	74.17	3.84 ↑
	KL-1 vs KL-3	93.17	95.87	2.70 ↑
	KL-1 vs KL-4	97.22	97.49	0.27 ↑
	KL-2 vs KL-3	94.87	95.91	1.04 ↑
	KL-2 vs KL-4	96.66	97.23	0.57 ↑
	KL-3 vs KL-4	95.11	95.99	0.88 ↑
Wang et al. [33]	KL-0 vs KL-1	69.08	70.21	1.13 ↑
	KL-0 vs KL-2	89.80	92.34	2.54 ↑
	KL-0 vs KL-3	98.75	99.11	0.36 ↑
	KL-1 vs KL-2	77.02	80.31	3.29 ↑
	KL-1 vs KL-3	96.84	97.93	1.09 ↑
	KL-1 vs KL-4	97.47	97.71	0.24 ↑
	KL-2 vs KL-3	95.53	96.59	1.06 ↑
	KL-2 vs KL-4	97.10	97.99	0.89 ↑
	KL-3 vs KL-4	95.88	96.25	0.37 ↑

* The augmented training set consists of the original training data and the synthesized intermediate frames.

performance improvements. As shown in Fig. 4, training on a dataset augmented with synthesized data has significantly improved the model’s ability to discern and differentiate between data points within the same class. Specifically, the reduction in intra-class distance (i.e., distance between data points within the same class) indicates that data points within each class are closer together in the feature space, resulting in denser and more defined clusters. Simultaneously, the preservation of inter-class distance (i.e., centre points of two classes) ensures that different classes remain distinct, preventing overlap and confusion. By achieving this balance, the augmented training set greatly improves the model’s generalization capabilities.

4.4.3 Expert assessment

Interventional Radiologists (IR) played a critical role in the evaluation process, particularly for the ambiguous KL-1 grade. To evaluate the accuracy and quality of the synthesized frames, three radiologists were involved. They provided expert assessments on KOA diagnosis based on the diagnostic criteria and their rich experience. As shown in Table 5, the quality (QTY) of the synthesized intermediate frames received an average score of 3.9 out of 5.0, indicating that the quality aligns with expert expectations. Regarding accuracy (Acc), which measures how well the synthesized frames match the expected labels, the overall average accuracy was a promising 89%, except for the KL-1 frames. On the other hand, an assessment of $x_S(\varphi_{\eta=0.25})$ frames reveals greater variability. The average accuracy drops to 62%, indicating that a substantial proportion of these frames did not correctly match the KL-1 label, as evidenced by the lowest accuracy score of only 50%, which could be attributed to the unclear definition of KL-1, leading to differing interpretations among the experts. Furthermore, the discrepancy in accuracy scores among the experts, ranging from as high as 74% to as low as 50%, may depend on their experience with extremely early-stage KOA, underscoring the subjective element inherent in medical image assessment. In contrast, the accuracy rates for $x_S(\varphi_{\eta=0.5})$, $x_S(\varphi_{\eta=0.75})$, and $x_S(\varphi_{\eta=1})$ frames are consistently high, often exceeding 85%, and remain relatively stable.

Overall, the proposed approach demonstrates strong generalization capability. The synthesized frames are not only technically sound but also clinically relevant, underscoring the potential of the approach to improve diagnostic accuracy and support clinical decision-making.

4.5 Discussion

In this study, we introduced a novel Diffusion-based Morphing Model (DMM) to synthesize intermediate frames between KL-0 and KL-4 knee radiographs. Leveraging the DDPM, our approach uniquely integrates diffusion and

Table 4: t-SNE scatter plots on the fixed validation set

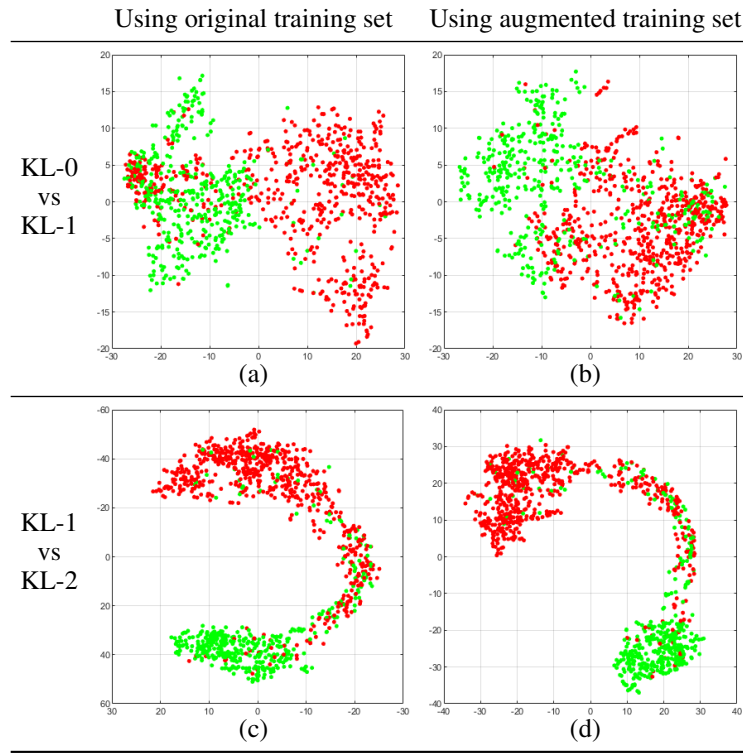


Table 5: Analysis of the experts' assessment

IR	Generated frames from KL-0							
	KL-1		KL-2		KL-3		KL-4	
	$x_S(\varphi_{\eta=0.25})$		$x_S(\varphi_{\eta=0.5})$		$x_S(\varphi_{\eta=0.75})$		$x_S(\varphi_{\eta=1})$	
	QTY	Acc	QTY	Acc	QTY	Acc	QTY	Acc
#1	3.8	62	4.2	89	4.1	88	4.3	91
#2	3.5	74	3.9	85	3.9	89	4.0	87
#3	3.4	50	4.0	83	3.7	85	4.2	93
Average	3.6	62	4.0	86	3.9	87	4.2	90

QTY: Subjective image quality rating out of 5.0.

Acc: The rate at which the labels of generated intermediate frames match the labels after expert assessment.

morphing processes to simulate the temporal evolution of KOA. The proposed hybrid loss strategy, which incorporates diffusion loss, morphing loss, and supervision loss, effectively facilitated the learning of spatial morphing information between the source and target images. Experimental evaluations have demonstrated the superiority of our approach in terms of PSNR and NMSE, highlighting its efficacy in synthesizing high-quality and accurate intermediate frames. Additionally, using these synthesized frames for data augmentation has significantly enhanced the performance of KOA classification tasks. During the test phase, positive assessments from radiology experts validated the clinical relevance of our approach, further confirming the high quality and precise grading of the synthesized images. There are several points to discuss.

4.5.1 Details of the hybrid loss

As presented in Section 2.3, the proposed hybrid loss consists of several components, each targeting specific aspects of the synthesized images. Specifically, the morphing loss J_{mph} is responsible for the morphing related to JSN and osteophytes, which is critical as their presence and severity can significantly influence the KL grade of the synthesized knee images. On the other hand, the supervision loss J_{sup} involves a supervision module that supervises the degree of the morphed JSN and osteophytes to ensure they accurately correspond to the respective KL grades at the anchor points images (i.e., $x_S(\varphi_{\eta=0.5})$ and $x_S(\varphi_{\eta=0.75})$).

4.5.2 Strengths and limitations

This study has several notable strengths. Clinically, enhancing the classification performance for early KOA diagnosis (i.e., KL-0 vs KL-2 and KL-1 vs KL-2) is highly significant, as it can guide patients to undertake timely physical interventions and potentially delay the onset and progression of KOA symptoms [44]. The synthesized intermediate frames are key in evaluating the effectiveness and accuracy of the morphing image registration algorithm as they provide insights into the algorithm’s behaviour at different stages. By analyzing these frames, researchers and practitioners can gain a deeper understanding of the morphing process. Moreover, to enhance the clinical applicability of our approach, a multi-faceted approach was conducted to evaluate the synthesized frames. We believe such a stable and interpretable model within a Computer-Aided Diagnosis (CAD) system can significantly enhance the trust and acceptance of deep learning methods among medical practitioners for clinical use. There are also several limitations in our study. Variations in imaging systems and software across different studies result in differences in detailed imaging data, such as Dots Per Inch (DPI), pixel size, and other specifics. Consequently, our proposed approach has not been validated across multiple datasets. These discrepancies could introduce biases in the synthesized intermediate frames, potentially affecting the model’s performance. Future work should focus on developing normalization or adaptation techniques to accommodate the variability in imaging data and automating hyper-parameter adjustments in the hybrid loss to broaden the applicability and enhance the efficiency of our approach.

5 Statements

This manuscript was prepared using data from the OAI. The views expressed in it are those of the authors and do not necessarily reflect the opinions of the OAI investigators, the National Institutes of Health (NIH), or the private funding partners.

6 Acknowledgements

The authors gratefully acknowledge the support of the National Institute of Arthritis and Musculoskeletal and Skin Diseases (NIAMS) of the NIH under award number K23AR084603, the Osteoarthritis Research Fund from Massachusetts General Hospital (MGH), Harvard Medical School (HMS).

References

- [1] Richard F Loeser, Steven R Goldring, Carla R Scanzello, and Mary B Goldring. Osteoarthritis: a disease of the joint as an organ. *Arthritis and rheumatism*, 64(6):1697, 2012.
- [2] Anna Litwic, Mark H. Edwards, Elaine M. Dennison, and Cyrus Cooper. Epidemiology and burden of osteoarthritis. *British Medical Bulletin*, 105(1):185–199, 01 2013.
- [3] Gurkirpal Singh, Jeffrey D Miller, Fleur H Lee, Dan Pettitt, and Mason W Russell. Prevalence of cardiovascular disease risk factors among us adults with self-reported osteoarthritis: data from the third national health and nutrition examination survey. *Population*, 7:17, 2002.

- [4] Juan C Mora, Rene Przkora, and Yenisel Cruz-Almeida. Knee osteoarthritis: pathophysiology and current treatment modalities. *Journal of pain research*, 11:2189, 2018.
- [5] Anita E Wluka, Cate B Lombard, and Flavia M Cicuttini. Tackling obesity in knee osteoarthritis. *Nature Reviews Rheumatology*, 9(4):225–235, 2013.
- [6] J. H. Kellgren and J. S. Lawrence. Radiological Assessment of Osteo-Arthrosis. *Annals of the Rheumatic Diseases*, 16(4):494, 1957.
- [7] Lior Shamir, Shari M Ling, William W Scott, Angelo Bos, Nikita Orlov, Tomasz J Macura, D Mark Eckley, Luigi Ferrucci, and Ilya G Goldberg. Knee x-ray image analysis method for automated detection of osteoarthritis. *IEEE Transactions on Biomedical Engineering*, 56(2):407–415, 2008.
- [8] Philippe Lambin, Ralph TH Leijenaar, Timo M Deist, Jurgen Peerlings, Evelyn EC De Jong, Janita Van Timmeren, Sebastian Sanduleanu, Ruben THM Larue, Aniek JG Even, Arthur Jochems, et al. Radiomics: the bridge between medical imaging and personalized medicine. *Nature reviews Clinical oncology*, 14(12):749–762, 2017.
- [9] Kun Hu, Wenhua Wu, Wei Li, Milena Simic, Albert Zomaya, and Zhiyong Wang. Adversarial evolving neural network for longitudinal knee osteoarthritis prediction. *IEEE transactions on medical imaging*, 41(11):3207–3217, 2022.
- [10] Marta Favero, Roberta Ramonda, Mary B Goldring, Steven R Goldring, and Leonardo Punzi. Early knee osteoarthritis. *RMD open*, 1(Suppl 1):e000062, 2015.
- [11] Armaghan Mahmoudian, L Stefan Lohmander, Ali Mobasheri, Martin Englund, and Frank P Luyten. Early-stage symptomatic osteoarthritis of the knee—time for action. *Nature Reviews Rheumatology*, 17(10):621–632, 2021.
- [12] Hayit Greenspan, Bram Van Ginneken, and Ronald M Summers. Guest editorial deep learning in medical imaging: Overview and future promise of an exciting new technique. *IEEE transactions on medical imaging*, 35(5):1153–1159, 2016.
- [13] Ian Goodfellow, Jean Pouget-Abadie, Mehdi Mirza, Bing Xu, David Warde-Farley, Sherjil Ozair, Aaron Courville, and Yoshua Bengio. Generative adversarial nets. *Advances in neural information processing systems*, 27, 2014.
- [14] Jonathan Ho, Ajay Jain, and Pieter Abbeel. Denoising diffusion probabilistic models. *Advances in neural information processing systems*, 33:6840–6851, 2020.
- [15] Youssef Kossale, Mohammed Airaj, and Aziz Darouichi. Mode collapse in generative adversarial networks: An overview. In *2022 8th International Conference on Optimization and Applications (ICOA)*, pages 1–6. IEEE, 2022.
- [16] Gustav Müller-Franzes, Jan Moritz Niehues, Firas Khader, Soroosh Tayebi Arasteh, Christoph Haarbuerger, Christiane Kuhl, Tianci Wang, Tianyu Han, Sven Nebelung, Jakob Nikolas Kather, et al. Diffusion probabilistic models beat gans on medical images. *arXiv preprint arXiv:2212.07501*, 2022.
- [17] Zhiye Guo, Jian Liu, Yanli Wang, Mengrui Chen, Duolin Wang, Dong Xu, and Jianlin Cheng. Diffusion models in bioinformatics: A new wave of deep learning revolution in action. *arXiv preprint arXiv:2302.10907*, 2023.
- [18] Rucha Deshpande, Muzaffer Özbey, Hua Li, Mark A Anastasio, and Frank J Brooks. Assessing the capacity of a denoising diffusion probabilistic model to reproduce spatial context. *IEEE Transactions on Medical Imaging*, 2024.
- [19] Kai Packhäuser, Lukas Folle, Florian Thamm, and Andreas Maier. Generation of anonymous chest radio-graphs using latent diffusion models for training thoracic abnormality classification systems. *arXiv preprint arXiv:2211.01323*, 2022.
- [20] Robin Rombach, Andreas Blattmann, Dominik Lorenz, Patrick Esser, and Björn Ommer. High-resolution image synthesis with latent diffusion models. In *Proceedings of the IEEE/CVF conference on computer vision and pattern recognition*, pages 10684–10695, 2022.
- [21] Walter HL Pinaya, Mark S Graham, Robert Gray, Pedro F Da Costa, Petru-Daniel Tudosiu, Paul Wright, Yee H Mah, Andrew D MacKinnon, James T Teo, Rolf Jager, et al. Fast unsupervised brain anomaly detection and segmentation with diffusion models. In *International Conference on Medical Image Computing and Computer-Assisted Intervention*, pages 705–714. Springer, 2022.
- [22] Tianqi Xiang, Wenjun Yue, Yiqun Lin, Jiewen Yang, Zhenkun Wang, and Xiaomeng Li. Diffcmr: Fast cardiac mri reconstruction with diffusion probabilistic models, 2023.
- [23] Lan Jiang, Ye Mao, Xi Chen, Xiangfeng Wang, and Chao Li. Cola-diff: Conditional latent diffusion model for multi-modal mri synthesis. *arXiv preprint arXiv:2303.14081*, 2023.

- [24] Firas Khader, Gustav Müller-Franzes, Soroosh Tayebi Arasteh, Tianyu Han, Christoph Haarburger, Maximilian Schulze-Hagen, Philipp Schad, Sandy Engelhardt, Bettina Baeßler, Sebastian Foersch, et al. Denoising diffusion probabilistic models for 3d medical image generation. *Scientific Reports*, 13(1):7303, 2023.
- [25] Jing Zou, Bingchen Gao, Youyi Song, and Jing Qin. A review of deep learning-based deformable medical image registration. *Frontiers in Oncology*, 12:1047215, 2022.
- [26] Johan Montagnat, Hervé Delingette, and Nicholas Ayache. A review of deformable surfaces: topology, geometry and deformation. *Image and vision computing*, 19(14):1023–1040, 2001.
- [27] G. Lester. The Osteoarthritis Initiative: A NIH Public–Private Partnership. *HSS Journal: The Musculoskeletal Journal of Hospital for Special Surgery*, 8(1):62–63, 2011.
- [28] Alexander Quinn Nichol and Prafulla Dhariwal. Improved denoising diffusion probabilistic models. In *International conference on machine learning*, pages 8162–8171. PMLR, 2021.
- [29] James R Norris. *Markov chains*. Number 2. Cambridge university press, 1998.
- [30] Olaf Ronneberger, Philipp Fischer, and Thomas Brox. U-net: Convolutional networks for biomedical image segmentation. In *Medical image computing and computer-assisted intervention–MICCAI 2015: 18th international conference, Munich, Germany, October 5-9, 2015, proceedings, part III 18*, pages 234–241. Springer, 2015.
- [31] Yuxin Wu and Kaiming He. Group normalization. In *Proceedings of the European conference on computer vision (ECCV)*, pages 3–19, 2018.
- [32] Max Jaderberg, Karen Simonyan, Andrew Zisserman, et al. Spatial transformer networks. *Advances in neural information processing systems*, 28, 2015.
- [33] Zhe Wang, Aladine Chetouani, and Rachid Jennane. Transformer with selective shuffled position embedding using roi-exchange strategy for early detection of knee osteoarthritis. *arXiv preprint arXiv:2304.08364*, 2023.
- [34] P. Chen, L. Gao, X. Shi, K. Allen, and L. Yang. Fully automatic knee osteoarthritis severity grading using deep neural networks with a novel ordinal loss. *Computerized Medical Imaging and Graphics*, 75:84–92, 2019.
- [35] J. Redmon and A. Farhadi. Yolo9000: better, faster, stronger. In *Proceedings of the IEEE conference on computer vision and pattern recognition*, pages 7263–7271, 2017.
- [36] Kaiming He, Xiangyu Zhang, Shaoqing Ren, and Jian Sun. Delving deep into rectifiers: Surpassing human-level performance on imagenet classification. In *Proceedings of the IEEE international conference on computer vision*, pages 1026–1034, 2015.
- [37] Diederik P. Kingma and Jimmy Ba. Adam: A method for stochastic optimization. *CoRR*, abs/1412.6980, 2015.
- [38] Adam Paszke, Sam Gross, Francisco Massa, Adam Lerer, James Bradbury, Gregory Chanan, Trevor Killeen, Zeming Lin, Natalia Gimelshein, Luca Antiga, Alban Desmaison, Andreas Köpf, Edward Yang, Zach DeVito, Martin Raison, Alykhan Tejani, Sasank Chilamkurthy, Benoit Steiner, Lu Fang, Junjie Bai, and Soumith Chintala. Pytorch: An imperative style, high-performance deep learning library, 2019.
- [39] Guha Balakrishnan, Amy Zhao, Mert R Sabuncu, John Guttag, and Adrian V Dalca. An unsupervised learning model for deformable medical image registration. In *Proceedings of the IEEE conference on computer vision and pattern recognition*, pages 9252–9260, 2018.
- [40] Adrian V Dalca, Guha Balakrishnan, John Guttag, and Mert R Sabuncu. Unsupervised learning for fast probabilistic diffeomorphic registration. In *Medical Image Computing and Computer Assisted Intervention–MICCAI 2018: 21st International Conference, Granada, Spain, September 16-20, 2018, Proceedings, Part I*, pages 729–738. Springer, 2018.
- [41] Boah Kim and Jong Chul Ye. Diffusion deformable model for 4d temporal medical image generation. In *International Conference on Medical Image Computing and Computer-Assisted Intervention*, pages 539–548. Springer, 2022.
- [42] A. Tiulpin, J. Thevenot, E. Rahtu, P. Lehenkari, and S. Saarakkala. Automatic knee osteoarthritis diagnosis from plain radiographs: A deep learning-based approach. *Scientific Reports*, 2018.
- [43] Laurens Van der Maaten and Geoffrey Hinton. Visualizing data using t-sne. *Journal of machine learning research*, 9(11), 2008.
- [44] Joanna Ledingham, Neil Snowden, and Zoe Ide. Diagnosis and early management of inflammatory arthritis. *Bmj*, 358, 2017.